Rapid Vapor-Phase Deposition of High-Mobility *p*-Type Buffer Layers on Perovskite Photovoltaics for Efficient Semi-Transparent Devices

Robert A. Jagt[†], Tahmida N. Huq[†], Sam A. Hill[†], Maung Thway[‖], Tianyuan Liu[‖], Mari Napari[†,‡],

Bart Roose[§], Krzysztof Gałkowski[§], Weiwei Li[⊥], Serena Fen Lin[‖], Samuel D. Stranks[§,¥], Judith L.

MacManus-Driscoll[†], Robert L. Z. Hoye[‖, †,*]

[†] *Department of Materials Science and Metallurgy, University of Cambridge, 27 Charles*

Babbage Road, Cambridge CB3 0FS, UK

[‖] *Solar Energy Research Institute of Singapore, National University of Singapore, Singapore*

117574

[§] *Department of Physics, Cavendish Laboratory, University of Cambridge, 19 JJ Thomson*

Avenue, Cambridge CB3 0HE, UK

[¥] *Department of Chemical Engineering and Biotechnology, University of Cambridge, Philippa*

Fawcett Drive, Cambridge CB3 0AS, UK

AUTHOR INFORMATION

[*]**Corresponding Author**

Email: r.hoye@imperial.ac.uk

ABSTRACT

Perovskite solar cells (PSCs) with transparent electrodes can be integrated with existing solar panels in tandem configurations to increase the power conversion efficiency. A critical layer in semi-transparent PSCs is the inorganic buffer layer, which protects the PSC against damage when the transparent electrode is sputtered on top. The development of *n-i-p* structured semi-transparent PSCs has been hampered by the lack of suitable *p*-type buffer layers. In this work we develop a *p*-type CuO_x buffer layer, which can be grown uniformly over the perovskite device without damaging the perovskite or organic hole transport layers. The CuO_x layer has high hole mobility (4.3 ± 2 cm² V^{-1} s^{-1}), high transmittance (>95%), and a suitable ionization potential for hole extraction (5.3 ± 0.2 eV). Semi-transparent PSCs with efficiencies up to 16.7% are achieved using the CuO_x buffer layer. Our work demonstrates a new approach to integrate *n-i-p* structured PSCs into tandem configurations, as well as enable the development of other devices that need high quality, protective *p*-type layers.

TOC GRAPHICS
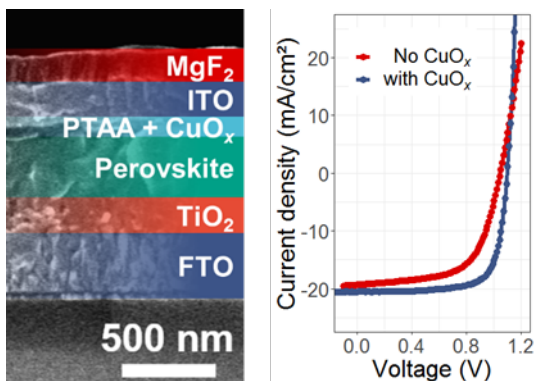
MAIN TEXT

Over the past decade, lead-halide perovskites have gained significant attention for optoelectronic applications, such as photovoltaics,[1] light-emitting diodes,[2] lasers,[3] X-ray/photon detectors[4,5] and water splitting.[6] These materials have the general formula ABX_3, where A is a monovalent cation (*e.g.*, $CH_3NH_3^+$), B a divalent cation (Pb^{2+}) and X a halide (I^-, Br^-, Cl^-). By changing the composition on the A, B and X sites, the band gap can be tuned from 1.2 eV to above 3.2 eV.[7–9] The ability to finely tune the band gap over a wide range, together with the ability to achieve long diffusion lengths using low-cost solution-based fabrication methods,[10] make lead-halide perovskites promising for applications in tandem photovoltaics, both as the top-cell (*e.g.* over silicon)[11] or in all-perovskite tandem solar cells (using a lead-tin perovskite bottom-cell).[7,12] The tandem configuration requires the perovskite top-cell to have transparent electrodes on both sides (*i.e.*, a semi-transparent device).

A key component in semi-transparent perovskite devices is an inorganic buffer layer that mechanically protects the perovskite sub-cell from damage when the transparent electrode is deposited on top by sputtering.[11,13–16] Unlike thermal evaporation of metal electrodes, sputtering can damage organic charge transport layers and the lead-halide perovskite film itself due to the high kinetic energy of the atomic species ($10–10^2$ eV for sputtering, compared to tens of meV for evaporation).[17] A wide range of *n*-type oxides have been developed, which have been integrated between the electron transport layer of *p-i-n* structured perovskite top-cells and the sputtered transparent conducting oxide (TCO). These materials include SnO_2,[13] zinc tin oxide (ZTO),[11] TiO_2, ZnO,[18] Al-doped ZnO[19] and indium doped ZnO (IZO).[20] These wide band gap *n*-type oxides have been shown to protect the perovskite top-cells from sputter damage, transmit visible and near-

infrared light and enable efficient electron extraction. As a result, efficient semi-transparent perovskite top-cells with low near-infrared optical losses have been achieved, which have been critical for the rapid development of perovskite-based tandems to a certified power conversion efficiency (PCE) of 29.1%, which already exceeds the record PCE of silicon single-junction devices (26.7%).[1]

However, there are currently no *p*-type oxide buffer layers demonstrated in *n-i-p* structured semi-transparent perovskite top-cells to protect the hole transport and perovskite layers from sputter damage. There are several reasons to integrate *n-i-p* structured perovskite solar cells in a semi-transparent architecture. Firstly, single junction *n-i-p* structured solar cells with evaporated opaque top electrodes have consistently outperformed their *p-i-n* counterparts (every entry on the NREL chart for the certified record efficiency perovskite solar cell to date is from an *n-i-p* structured device[1]), yet this has so far not been reflected in the performance of semi-transparent devices.[21–23] Secondly, two-terminal tandems using *n*-type silicon bottom cells with hole selective contacts on top require an *n-i-p* structured perovskite top-cell (although this does not apply to silicon heterojunction cells). These will be important because *n*-type silicon is gaining an increasing share of the silicon wafer market owing to higher PV efficiencies than *p*-type silicon PVs.[24] Thirdly, *n-i-p* structured semi-transparent perovskite devices are needed for photoanodes in solar-fuel production, which can be combined with the already-developed *p-i-n* structured perovskite photocathodes for bias-free water splitting.[25] Buffer layers to protect *n-i-p* semi-transparent devices are also needed in multi-junction light-emitting diodes (LEDs; *e.g.*, for white-light devices), transparent complementary metal oxide semiconductor (CMOS) circuits, and for performing spectroscopy on devices under operation.

The difficulty in achieving *p*-type semiconductors with equivalent performance to *n*-type semiconductors arises due to the formation energy of donor defects (such as oxygen vacancies) in oxides being low compared to acceptor defects (such as cation vacancies), making *n*-type oxides more common. Due to the current lack of *p*-type oxide buffer layers for semi-transparent devices, the majority of researchers utilize MoO_x (a high work function *n*-type oxide) as a buffer layer.[12,15,16,22,26,27] However MoO_x reacts strongly with the lead-halide perovskite, hampering the long-term stability.[28,29] Researchers are actively searching for alternatives, but these efforts have mainly focussed on other high work function *n*-type oxides. Raiford *et al*. recently investigated *n*-type VO_x as a buffer layer. They obtained semi-transparent *n-i-p* devices with 1000 h stability, but the maximum PCE was 14%.[30] Another option is *n*-type WO_x. But Hou *et al*. reported that it was necessary to dope WO_x with Ta, which decreased the near-infrared transmittance and would therefore result in increased parasitic optical losses to the bottom cell in a tandem.[28] Park *et al*. recently demonstrated that a more effective approach was to modify WO_x by evaporating a thin 9 nm layer of NbO_y on top. But fine nanometer-level control over the thickness of NbO_y was found to be essential to avoid decreasing the transmittance, and also to avoid thermally-induced degradation of the organic hole transport layer during the deposition of the oxide by evaporation, in which temperatures could reach 80 °C.[31]

Owing to the limitations of high work function *n*-type oxides, developing *p*-type oxide buffer layers is critical. Viable materials can be found by looking to the *p*-type oxides used as hole transport layers beneath the perovskite in *p-i-n* structured devices. Two popular materials are NiO_x and Cu_2O, with both materials shown to not accelerate the degradation of the perovskite when in

direct contact, unlike MoO_x.[28,29,32–34] In particular, both oxides have valence band maxima that are well aligned with that of the perovskite and do not require the addition of dopants to efficiently extract holes (unlike many organic hole transport layers), which is conducive to stable device performance.[28] But depositing these oxides on the top of the perovskite device stack rather than beneath it poses additional constraints compared to depositing *p*-type oxide layers on glass or conducting glass substrates. Due to the limited thermal stability of perovskites, the deposition method must be able to achieve the film requirements (high mobility, high transmittance, pinhole-free morphology) at low deposition temperatures without the use of energetic particles during oxide growth.[30,35] This would rule out most of the methods that have been used to deposit NiO_x and Cu_2O, which require high-temperature post-annealing for optimal properties (*e.g.*, from sol-gel processing[36]) or involve energetic particles (*e.g.*, reactive sputtering[37]). Whilst the perovskite could be protected to a limited extent by increasing the thickness of the organic hole transport layer,[38] this strategy would lead to increased parasitic optical losses and increased series resistance that would reduce the efficiency of the semi-transparent perovskite cell, as well as the silicon bottom cell in a tandem. Achieving high quality *p*-type oxides grown using deposition conditions that are compatible with the perovskite covered with only a thin organic hole transport layer is a critical challenge.

In this work we aim to develop a *p*-type buffer layer for semi-transparent *n-i-p* structured perovskite solar cells as an alternative to high workfunction *n*-type oxides. We focus on CuO_x as the *p*-type material and the key challenge we aim to overcome is to grow this layer over the perovskite device stack with high density, uniformity and transmittance, but without damaging the perovskite and PTAA (poly[bis(4-phenyl)(2,4,6-trimethylphenyl)amine]) layers. We investigate

the influence of the growth conditions of CuO_x from the vapor phase on the structural, electrical and electronic properties of the films and their suitability for applications as a buffer layer. In particular, we use structural and spectroscopic characterization to probe whether CuO_x degrades the bulk or interfaces of the perovskite films. We test the CuO_x layer in semi-transparent *n-i-p* structured devices, and focus on understanding whether sputter damage to the perovskite and organic hole transport layers can be further reduced through thermalized deposition of the TCO, whilst not sacrificing the TCO material's carrier and optical properties. These semi-transparent devices are used as top-cells in four-terminal tandems with two types of silicon bottom cells that are industrially-relevant: *p*-type passivated emitter rear contact (PERC) and *n*-type silicon cells with polycrystalline silicon passivation.[39,40]

We chose to focus on CuO_x rather than NiO_x because Cu_2O can be grown at temperatures below 200 °C by chemical vapor deposition (CVD) or atomic layer deposition (ALD),[41] which are soft growth methods, unlike sputtering. We grew the CuO_x layers by atmospheric pressure chemical vapor deposition (AP-CVD). A detailed description of AP-CVD can be found in Ref. 42. In brief, the metal precursor and oxidant are introduced to separate channels in a gas manifold, which guides the vapor-phase precursors vertically down to the substrate. The substrate is held by a platen, which oscillates the substrate beneath the gas channels repeatedly to grow the oxide layer-by-layer. This process is analogous to 'printing' the metal oxide, in which the thickness of the oxide is controlled by the number of layers and exposure time of the substrate to the precursors. Allyloxytrimethylsilyl Hexafluoroacetylacetonate Copper(I) (Cupraselect®) was used as the metal precursor and water vapor as the oxidant. The deposition temperatures were varied between 100 ºC and 150 ºC (refer to the Experimental section in the SI). Based on prior work with *n*-type AP-CVD oxides grown

over lead-halide perovskites, this is the temperature range that was expected to be compatible with the perovskites.[43] By changing the exposure time per cycle, it was found that there was a linear dependence of the growth rate with exposure time, showing the growth mechanism to be chemical vapor deposition rather than atomic layer deposition. The growth rate at 100 °C and 150 °C were similar, at 1.30 nm min^{-1} and 1.34 nm min^{-1} respectively (Fig. S1, SI), which are an order of magnitude higher than for conventional ALD.[44] Moreover, unlike conventional ALD or sputtering, AP-CVD grows oxides without vacuum, which further shortens the total time required to grow the oxide to minutes rather than >1 h.[41] We found that our AP-CVD films can be grown over large areas (>6 cm^2 deposition area, Fig. 1a), with a thickness variation of only 5% (one standard deviation relative to the mean thickness, Fig. 1b), making this technique suitable to scale up for large area devices.
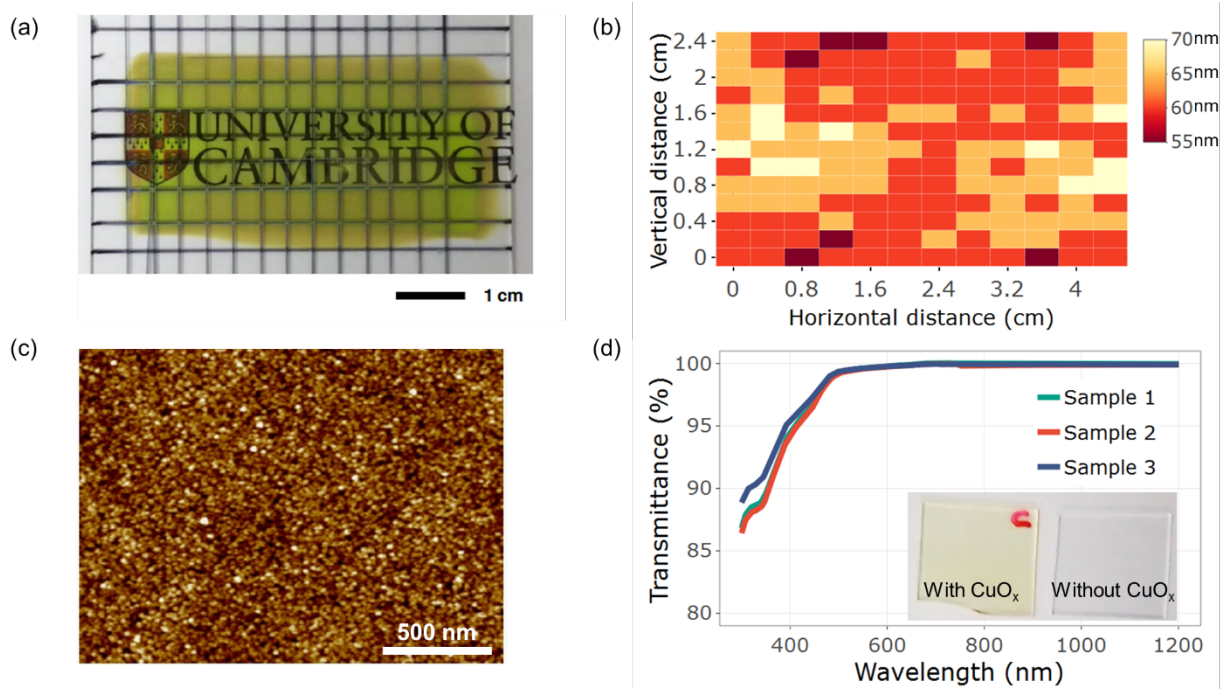
Figure 1. Properties of AP-CVD CuO$_x$ grown onto glass. Analysis of 60 nm thick CuO$_x$: (a) Photograph of 60 nm CuO$_x$ grown at 100 °C onto glass, and (b) the measured thicknesses over the

deposition area. Analysis of CuO$_x$ with a thickness of 3 nm (determined from growth rate): (c) Atomic force microscopy image of CuO$_x$ grown onto glass (root mean square roughness 0.64 nm) and (d) corresponding measured transmittance. The transmittance of the film is corrected for the absorption of the glass. The inset shows photographs of borosilicate glass with (left) and without (right) the CuO$_x$ layer.

The phase stability of Cu$_2$O is narrow and careful control of the processing conditions is required to avoid impurity phases such as Cu metal or CuO.[45,46] But although CuO is more thermodynamically stable at atmospheric pressure, phase-pure Cu$_2$O can still be reproducibly achieved if the deposition temperatures are low (<320 °C), when reaction kinetics play a sizeable role.[41,47] X-ray diffraction measurements showed the films (50 nm thick) to be phase-pure cubic Cu$_2$O, with no crystalline CuO phase-impurities detected (Fig. S2, SI). Furthermore, we found the films to remain phase-pure Cu$_2$O after four days of storage in ambient air (Fig. S3, SI). This is consistent with results other groups have reported on ALD Cu$_2$O, in which no structural or compositional degradation occurred after storage in air.[41] X-ray photoemission spectroscopy (XPS) measurements confirm the films to contain Cu in the 1+ oxidation state, with no 2+ satellites observed on the surface (Fig. S4, SI). After sputtering through the surface contaminant layer, we can still detect a very small C 1s core level peak, probably originating from the metal precursor. We measured the bulk composition in detail using time-of-flight elastic recoil detection analysis (ToF-ERDA) and found the C content to be low, at 1.9±0.2 at.% (100 °C growth temperature), decreasing to 0.7±0.1 at.% for films grown at 150 °C (Table S1 and Fig. S5, SI). We measured the bulk ratio of O to Cu (*i.e.*, x value in CuO$_x$) to be 0.4 across all deposition temperatures (specifically 0.39±0.03 for the film deposited at 100 °C), which is sub-stoichiometric for Cu$_2$O (or CuO$_{0.5}$).

Lastly, through ultraviolet–visible spectrophotometry we measured the optical bandgap to be 2.44 eV (Fig. S6, SI), in line with other experimental work.[48] Note that CuO_x has a direct forbidden band gap of 2.07 eV (as measured form the photoluminescence).[38]

We investigated whether the growth of CuO_x onto perovskite devices results in bulk structural damage. To test this, we measured the X-ray diffraction (XRD) pattern, before and after CuO_x deposition, of a triple-cation lead-halide perovskite film[1] coated with PTAA and deposited on top of a glass substrate. The as-grown triple-cation perovskites have residual lead iodide (PbI_2) present, which may be beneficial for passivation purposes.[49] Depositing CuO_x for 100 cycles (approximately 3 nm thickness, as determined based on the growth rate; total deposition time <2 min) at 100 °C over the perovskite/PTAA films resulted in no significant increase in the bulk PbI_2 peak intensity (Fig. S7, SI). However, at 125 °C, the PbI_2 peak became significantly more intense, indicating the decomposition of the perovskite. We therefore focussed on films grown at 100 °C.

To study the morphology of the AP-CVD CuO_x film, we deposited onto O_2 plasma treated glass at 100 °C. The atomic force microscopy (AFM) image shows the film to be devoid of pinholes (Fig. 1c), with a root mean square roughness of 0.64 nm, whereas the bare glass has a root mean square roughness of 0.21 nm (Fig. S1, SI). Owing to the thin nature of these films, the transmittance was >95% over the entire visible and near-infrared wavelength range (Fig. 1d), and was close to

---

[1] $(Cs_{0.05}(MA_{0.17}FA_{0.83})_{0.95}Pb(I_{0.83}Br_{0.17})_3)$, MA = $CH_3NH_3^+$, FA = $CH(NH_2)_2^+$.

100% for near-infrared wavelengths. The CuO_x films grown for <2 min in atmospheric conditions are therefore dense, pinhole-free and give negligible parasitic optical losses.

Hall measurements of 100 nm CuO_x grown on glass at 100 °C confirmed the films to be *p*-type with an average measured Hall mobility of 4.3 ± 2 cm² V⁻¹ s⁻¹ and a carrier concentration of (2.0 ± 1.1)×10^{15} cm⁻³. The Hall mobility of CuO_x is orders of magnitude higher than the mobilities of organic hole transport layers used in perovskite solar cells, such as PTAA (~10^{-3} cm² V⁻¹ s⁻¹) and spiro-OMeTAD (~10^{-4} cm² V⁻¹ s⁻¹).[50] Notably, there is no need to dope the CuO_x layer to improve its conductivity, which is in contrast to these organic materials.

We investigated whether CuO_x grown at 100 °C has a suitable band alignment with perovskite devices. CuO_x was grown onto silicon substrates coated with Au. Using Kelvin probe measurements, we found the work function to be a stable value of 4.9 ± 0.1 eV (Fig. S8, SI). Combined with a Fermi level to valence band offset of 0.40 ± 0.1 eV from XPS measurements (Fig. S8, SI), the ionization potential of CuO_x was found to be 5.3 ± 0.2 eV. This is very well matched with the highest occupied molecular orbital (HOMO) of PTAA and the perovskite valence band maximum, making the AP-CVD CuO_x well suited as buffer layer in *n-i-p* structured perovskite devices.

To determine whether depositing CuO_x on perovskites and perovskite/PTAA stacks used in devices resulted in increased non-radiative recombination, we measured the photoluminescence (PL) decay. Any non-radiative recombination will result in additional parasitic recombination pathways of carriers to lower-energy states, leading to lower quasi-Fermi levels and effective

charge densities and, ultimately, lower open-circuit voltages.[51] Notably, directly depositing CuO_x on lead-halide perovskites at 100 °C resulted in similar PL decay kinetics as the pristine perovskite itself (Fig. 2a), suggesting the deposition of CuO_x to not degrade the surface of the perovskite or introduce traps at the interface. Similarly, the PL decay kinetics of perovskite/PTAA bilayers were unchanged with the CuO_x layer added (Fig. 2b), showing CuO_x to also not damage the thermally-sensitive PTAA layer, in spite of growth in air. Lastly the PL decay was not quenched when the tin-doped indium oxide (ITO) was deposited on top (Fig. 2c&d). The absence of further PL quenching at open-circuit measurement conditions after the addition of the CuO_x layer here implies that no additional non-radiative pathways were introduced, which would otherwise be detrimental for device performance.[52]
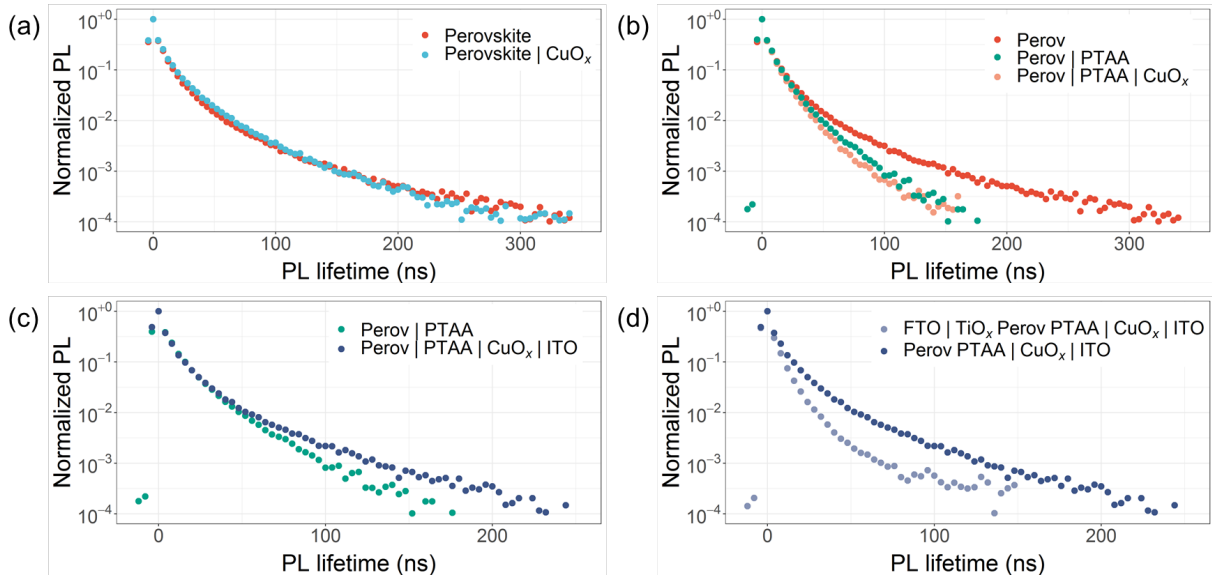
Figure 2. Measured photoluminescence lifetime for different device stack configurations (device configurations indicated in the figure legends).

The transparent electrode, ITO, was deposited by DC magnetron sputtering. For details see the Experimental section in the SI. The 320 nm thick ITO film had a measured Hall mobility of $35.6 \; cm^2 \, V^{-1} \, s^{-1}$ and a carrier concentration of $9.0 \times 10^{20} \, cm^{-3}$, with a sheet resistance of $9.2 \; \Omega \, \square^{-1}$.

Having found the CuO_x layer to be of high quality and not damage the perovskite/PTAA stack, we investigated its effect on device performance and whether it can be used to protect against sputter damage. The band structure of the device stack, along with a corresponding cross-sectional SEM image of the semi-transparent devices is shown in Fig. 3a&b, respectively. The top-down scanning electron microscopy images are shown in Fig. S9, SI. We observed the morphology of the perovskite/PTAA stack without and with the CuO_x to be the same, suggesting the CuO_x layer to be conformal. This is consistent with previous work, in which it was shown through transmission electron microscopy that CuO_x grown by AP-CVD is conformal to high-aspect ratio nanorods.[53]
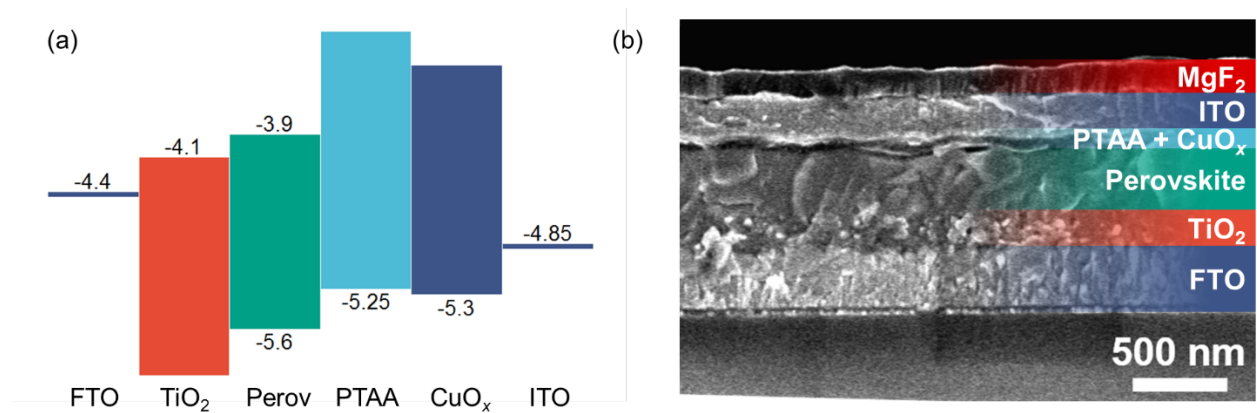
Figure 3. (a) Band structure of the semi-transparent perovskite device. The CuO_x and ITO band positions were measured by Kelvin probe and X-ray photoemission spectroscopy. The band positions of the other layers were obtained from the literature.[50,54] (b) Cross-sectional scanning electron microscopy image of the semi-transparent device. The device structure was MgF_2/glass/FTO/c-TiO_2/mp-TiO_2/$Cs_{0.05}(MA_{0.17}FA_{0.83})_{0.95}Pb(I_{0.83}Br_{0.17})_3$/ PTAA/$CuO_x$/ITO/$MgF_2$.

Next we investigated the performance of the CuO_x buffer layer in devices. In all device measurements the devices were illuminated from the substrate (glass/FTO/TiO_x) side. The control *n-i-p* structured devices with opaque Au top electrodes had a standard efficiency of up to 19.9% (median of 17.4%, Fig. S10, SI). When the Au top electrode was replaced by ITO directly sputtered on the PTAA layer, the device efficiency dropped significantly. The maximum efficiency achieved without a buffer layer was 12.5%. The low efficiency was mostly due to a low fill factor ($< 61\%$, see Fig. 4a). Introducing a CuO_x buffer layer greatly improved the device performance. The optimum CuO_x layer thickness was found to be 3-5 nm (Fig. S11, SI). Thicker layers led to reduced performance, possibly due to the thicker films having sub-optical electronic properties or due to the longer deposition time (>6 min) resulting in thermally-induced degradation of the perovskite surface buried beneath the PTAA layer. The median and maximum PCEs were both higher (13.9% (median) / 16.7% (maximum)) for the semi-transparent devices with 3 nm CuO_x buffer layers than those with MoO_x buffer layers (13.7% (median) / 16.1% (maximum)). This indicates that using 3 nm CuO_x (or indeed 5 nm CuO_x) resulted in no damage to the perovskite. Please refer to Fig. 4, Table 1, Fig. S10 and Fig. S11, SI. In the champion semi-transparent device with a CuO_x buffer layer, the integrated EQE (20.3 mA cm^{-2}) matched with the measured short circuit current density (20.6 mA cm^{-2}, see Fig. 4d).

The performance of our champion semi-transparent device is comparable to the best opaque-electrode devices using Cu/Cu_2O by Chen *et al.*,[38] and is also comparable to the state-of-the-art performance in semi-transparent perovskite devices (Table S2, SI).[11,16,21,22,55–59] The AP-CVD CuO_x therefore allows the perovskite coated with only a thin organic charge transport layer to be

protected from sputter damage, and also enables high transmittance and performance to be simultaneously achieved. We expect that our approach would be compatible with other perovskite device structures with comparable thermal stability, and could in the future be used, for example, with *n-i-p* structured perovskite devices with optimal interface passivation that could achieve higher efficiencies.
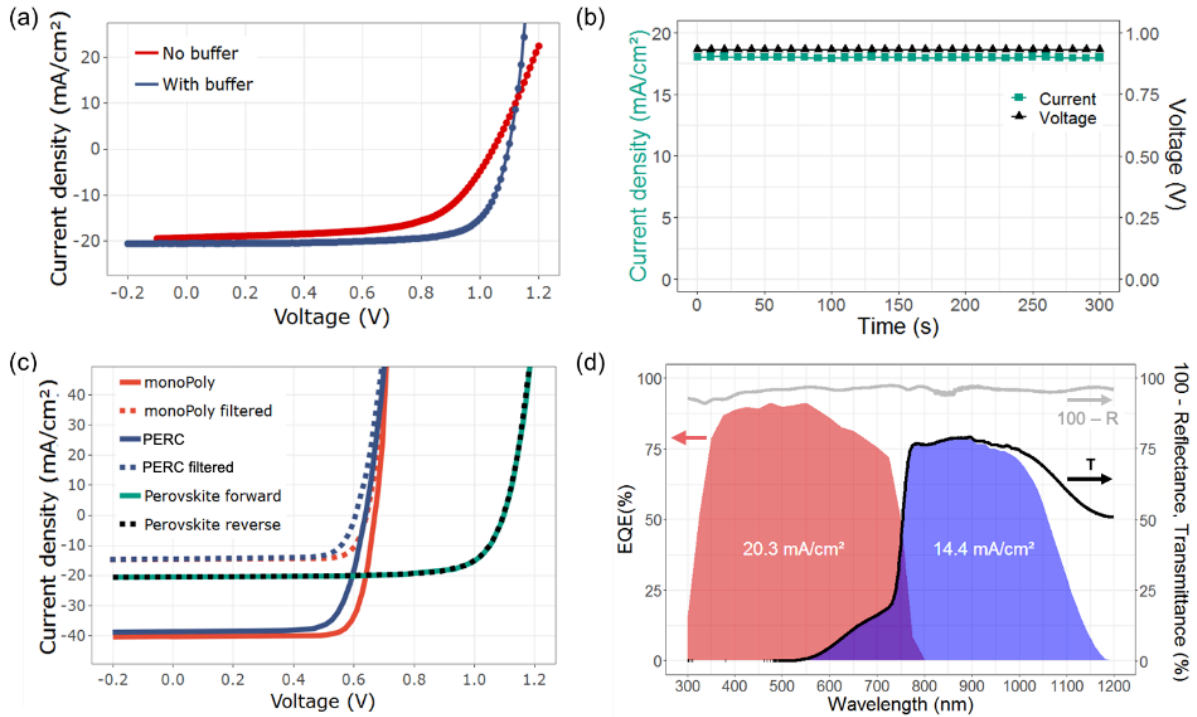
Figure 4. (a) Measured reverse current density – voltage curve of the best devices with and without a CuO$_x$ buffer layer. (b) Maximum power point tracking of the current density and voltage of the champion device with a CuO$_x$ buffer layer. (c) Measured current density – voltage curves of the semi-transparent perovskite solar cell and the unfiltered and filtered Si bottom cell. (d) Measured external quantum efficiency (EQE) of the perovskite solar cells (red) and of the filtered silicon bottom cell (blue). EQE values are read from the left axis. The transmittance (%) and (100%-Reflectance(%)) of the solar cell device stack are depicted by a black line and gray lines, and can be read from the right axis.

We applied our efficient semi-transparent perovskite devices as top-cells in four-terminal tandems with silicon. The four-terminal tandem efficiency was determined using standard approaches. That is, we measured the semi-transparent perovskite device and the perovskite-filtered silicon bottom cell separately, then added their efficiencies together. The silicon bottom cell was filtered with a 4 cm^2 semi-transparent perovskite top-cell, which was illuminated through its glass side, consistent with our measurements of the semi-transparent perovskite top-cell. More efficient bottom cells usually result in lower efficiency gains despite an overall higher tandem efficiency. We fabricated a *p*-type passivated emitter rear contact (PERC) bottom cell, which is commonly used in industry, with an unfiltered efficiency of 18.5% (Table 1). The PERC cell was optimized to function as a bottom cell in a four terminal tandem.[39] The measured bottom cell efficiency was 6.70% when filtered with the perovskite top-cell, which is close to our calculated value based on the transmittance of the perovskite filter (refer to Eq. S1&S2, SI). Adding our semi-transparent perovskite top-cell results in an efficiency gain of 4.95% in the four-terminal tandem compared to the unfiltered silicon single-junction PERC cell.

We also made four-terminal tandems with *n*-type silicon bottom cells with passivating poly-silicon layers.[40] The *n*-type monoPoly™ silicon solar cells are highly industrially relevant due to their simple fabrication process. The structure can be realized with a lean 7-step processing sequence.[40] Owing to the higher performance of the *n*-type bottom cells, we achieved a four-terminal tandem efficiency of 24.4%, with an overall gain of 2.78% over the silicon bottom cell (Table 1). This shows the future potential of making two-terminal tandems with these *n*-type bottom cells, in which it is critical that the top-cell has an *n-i-p* structure. We also note that if we

were to use the record-efficiency silicon heterojunction interdigitated back contact solar cell as our bottom cell,[61] we would expect to achieve a tandem efficiency of up to 27% (refer to Eq. S1&S2, SI). This would be comparable to the highest four-terminal tandem efficiency reported for any perovskite top-cell structure.[16,59,62] Finally, we note that in a two-terminal tandem, the perovskite top-cell would be illuminated through the sputtered ITO top electrode. Although we only measured our semi-transparent devices from the substrate side in this work, the CuO_x layer has negligible parasitic optical losses (Fig. 1d). We would therefore expect that the use of the dense, ultrathin CuO_x in a perovskite top-cell that has been optimized to minimize reflectance losses would result in the semi-transparent top-cell having comparable efficiencies when illuminated from either side.[63]

Table 1. Performance of champion single-junction silicon bottom cells measured directly under 1 sun radiation, and when filtered with the semi-transparent perovskite top-cell. The four-terminal tandem performance of the silicon devices when combined with the champion 16.7%-efficient semi-transparent perovskite device is also shown

	J_{sc} (mA cm^{-2})	V_{oc} (mV)	FF (%)	PCE (%)
Semi-transparent Perovskite	20.63	1100.0	73.66	16.72
c-Si PERC	38.78	632.7	75.26	18.47
c-Si PERC filtered	14.54	597.9	77.09	6.70
Tandem with c-Si PERC				23.42

monoPoly™ c-Si	40.39	664.2	80.45	21.58
monoPoly™ c-Si filtered	14.73	634.1	81.84	7.64
Tandem with monoPoly™ c-Si				24.36

Sputter damage can occur to the perovskite device despite the presence of a buffer layer if the sputtering conditions are not carefully optimized.[64] The damage is due to the high kinetic energy of the sputtered particles. The conductance and transmittance of the TCO and the extent of damage to the solar cells are highly dependent on the deposition power, source to substrate distance and working pressure.[65] Typically TCOs are deposited at low pressure to maximize the carrier concentration.[11,13,16,19] However, decreasing the pressure also increases the kinetic energy of the atomic species arriving at the substrate surface, inducing more sputter damage. Using standard kinetic gas theory, it is possible to calculate the distance the atomic species need to travel before their kinetic energy is reduced to the kinetic energy of the background gas. See SI for more details. This distance is called the thermalization distance and is depicted in Fig. 5 as a function of sputter pressure.

In this work the sputter pressure and source to substrate distance were 2 Pa and 5 cm. The voltage across the target and chamber at different pressures is shown in Fig. S12, SI. As can be seen in Fig. 5 the thermalization distance for the various atoms is smaller than the source to substrate distance. Hence the atomic species originating from the target have slowed down to the background gas temperature. The TCO still had high carrier concentration and mobility values of $9.0 \times 10^{20} \, cm^{-3}$ and $35.6 \, cm^2 \, V^{-1} \, s^{-1}$. In other works, the background pressure is typically set between

0.2 and 0.4 Pa. The thermalization distance of the different atoms is then between 20 and 30 cm and therefore sputtering is performed in the ballistic regime where the kinetic energy of the atomic species is still significantly higher than the kinetic energy of the background gas (see also Fig. S14–S16 and in Section S4, SI). It is hypothesized that the increased background pressure reduces interfacial damage. In this work, depositing at lower pressure caused the TCO films to delaminate due to the increased compressive stresses (see Fig. S13, SI). Further work is needed to assess the impact of sputter pressure on interfacial damage between the TCO and transport or buffer layers.
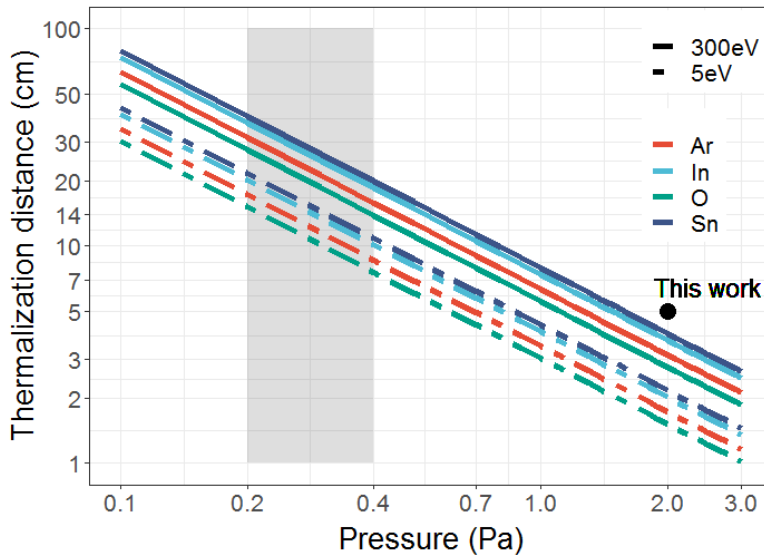
Figure 5. Calculated thermalization distance for different atomic species (In, Sn, O, Ar) and different initial kinetic energies (5 eV and 300 eV) as a function of pressure. The grey area indicates typical employed sputtering pressures. The black circle at (2 Pa, 5 cm) indicates the pressure and the source to substrate distance at which the ITO was sputtered here.

In summary, the current lack of *p*-type buffer layers hampers the development of semi-transparent *n-i-p* structured perovskite devices. In this work, we developed thin high mobility *p*-type CuO_x films, which can be grown at low temperatures. This enabled us to achieve *n-i-p* semi-transparent devices with state-of-the-art performance and high near-infrared transmittance, enabling high efficiency gains when used as top-cells in four-terminal tandems with silicon bottom cells. The *p*-type oxide we used is CuO_x ($x = 0.39 \pm 0.03$ from ToF-ERDA measurements) grown by AP-CVD with a high deposition rate (1.3 nm min^{-1}), without vacuum, and with high film uniformity (5% thickness variation over >6 cm^2 deposition area) and hole mobility (4.3 ± 2 cm^2 V^{-1} s^{-1}) without requiring dopants. Thin 3 nm films were found to be pinhole-free with >95% transmittance to visible and near-infrared light. XRD and time-resolved photoluminescence showed that growing CuO_x at 100 °C on perovskite devices resulted in no bulk structural damage or extra non-radiative recombination at the interface. The thin CuO_x was found to be sufficient to protect the perovskite device from sputter damage. The semi-transparent devices utilizing the CuO_x buffer layer were found to be more efficient than the control with MoO_x. The CuO_x buffer layer can easily be integrated in device structures with high efficiencies. Our work opens up a new avenue to exploit the most efficient perovskite device architecture (*n-i-p*) in semi-transparent devices and in top-cells for tandem photovoltaics. More broadly, these semi-transparent devices could be used in photoanodes for bias-free solar fuel generation, multi-junction white-light LEDs and other transparent devices and electronic circuits. Our work also motivates the uptake and further development of *p*-type buffer layers in semi-transparent perovskite devices.

ASSOCIATED CONTENT

Supporting Information

The Supporting Information is available free of charge on the ACS Publications website at DOI:XXXX

Experimental section, supporting growth curves for AP-CVD CuO_x, supporting morphology, phase and composition measurements, supporting Tauc plots for the triple-cation perovskite and CuO_x films, supporting band structure measurements, supporting device measurements and comparison of the performance with the literature, details of the method for calculating the efficiency of four terminal tandems, and derivation of the thermalization distance (PDF)

AUTHOR INFORMATION

Corresponding Author

Email: r.hoye@imperial.ac.uk (R. L. Z. Hoye)

Present Addresses

‡ *Present address: Zepler Institute for Photonics and Nanoelectronics, University of Southampton, University Road, Southampton SO17 1BJ, UK*

‼ *Present address: Department of Materials, Imperial College London, Exhibition Road, London SW7 2AZ, UK*

Notes

The authors declare no competing interests.

ACKNOWLEDGMENT

REFERENCES

(1)   Best Research-Cell Efficiencies. *National Renewable Enery Laboratory*. https://doi.org/https://www.nrel.gov/pv/assets/pdfs/best-research-cell-efficiencies.20190923.pdf.

(2)   Lin, K.; Xing, J.; Quan, L. N.; de Arquer, F. P. G.; Gong, X.; Lu, J.; Xie, L.; Zhao, W.; Zhang, D.; Yan, C.; Li, W.; Liu, X.; Lu, Y.; Kirman, J.; Sargent, E. H.; Xiong, Q.; Wei, Z. Perovskite Light-Emitting Diodes with External Quantum Efficiency Exceeding 20 per

Cent. *Nature* **2018**, *562* (7726), 245–248. https://doi.org/10.1038/s41586-018-0575-3.

(3)   Zhang, N.; Fan, Y.; Wang, K.; Gu, Z.; Wang, Y.; Ge, L.; Xiao, S.; Song, Q. All-Optical Control of Lead Halide Perovskite Microlasers. *Nat. Commun.* **2019**, *10* , 1770. https://doi.org/10.1038/s41467-019-09876-6.

(4)   Wei, W.; Zhang, Y.; Xu, Q.; Wei, H.; Fang, Y.; Wang, Q.; Deng, Y.; Li, T.; Gruverman, A.; Cao, L.; Huang, J. Monolithic Integration of Hybrid Perovskite Single Crystals with Heterogenous Substrate for Highly Sensitive X-Ray Imaging. *Nat. Photon.* **2017**, *11* (5), 315–321. https://doi.org/10.1038/nphoton.2017.43.

(5)   Feng, J.; Gong, C.; Gao, H.; Wen, W.; Gong, Y.; Jiang, X.; Zhang, B.; Wu, Y.; Wu, Y.; Fu, H.; Jiang, L.; Zhang, X. Single-Crystalline Layered Metal-Halide Perovskite Nanowires for Ultrasensitive Photodetectors. *Nat. Electron.* **2018**, *1* (7), 404–410. https://doi.org/10.1038/s41928-018-0101-5.

(6)   Poli, I.; Hintermair, U.; Regue, M.; Kumar, S.; Sackville, E. V.; Baker, J.; Watson, T. M.; Eslava, S.; Cameron, P. J. Graphite-Protected CsPbBr 3 Perovskite Photoanodes Functionalised with Water Oxidation Catalyst for Oxygen Evolution in Water. *Nat. Commun.* **2019**, *10* , 2097. https://doi.org/10.1038/s41467-019-10124-0.

(7)   Eperon, G. E.; Leijtens, T.; Bush, K. A.; Prasanna, R.; Green, T.; Wang, J. T. W.; McMeekin, D. P.; Volonakis, G.; Milot, R. L.; May, R.; Palmstrom, A.; Slotcavage, D. J.; Belisle, R. A.; Patel, J. B.; Parrott, E. S.; Sutton, R. J.; Ma, W.; Moghadam, F.; Conings, B.; Babayigit, A.; Boyen, H. G.; Bent, S.; Giustino, F.; Herz, L. M.; Johnston, M. B.; McGehee, M. D.; Snaith, H. J. Perovskite-Perovskite Tandem Photovoltaics with Optimized Band Gaps. *Science* **2016**, *354* (6314), 861–865. https://doi.org/10.1126/science.aaf9717.

(8)   Unger, E. L.; Kegelmann, L.; Suchan, K.; Sörell, D.; Korte, L.; Albrecht, S. Roadmap and

Roadblocks for the Band Gap Tunability of Metal Halide Perovskites. *J. Mater. Chem. A* **2017**, *5* (23), 11401–11409. https://doi.org/10.1039/c7ta00404d.

(9)   Hoye, R. L. Z.; Lai, M. L.; Anaya, M.; Tong, Y.; Gałkowski, K.; Doherty, T.; Li, W.; Huq, T. N.; Mackowski, S.; Polavarapu, L.; Feldmann, J.; Macmanus-Driscoll, J. L.; Friend, R. H.; Urban, A. S.; Stranks, S. D. Identifying and Reducing Interfacial Losses to Enhance Color-Pure Electroluminescence in Blue-Emitting Perovskite Nanoplatelet Light-Emitting Diodes. *ACS Energy Lett.* **2019**, *4* (5), 1181–1188. https://doi.org/10.1021/acsenergylett.9b00571.

(10)   Stranks, S. D.; Eperon, G. E.; Grancini, G.; Menelaou, C.; Alcocer, M. J. P.; Leijtens, T.; Herz, L. M.; Petrozza, A.; Snaith, H. J. Electron-Hole Diffusion Lengths Exceeding 1 Micrometer in an Organometal Trihalide Perovskite Absorber. *Science* **2013**, *342* (6156), 341–345.

(11)   Fu, F.; Feurer, T.; Weiss, T. P.; Pisoni, S.; Avancini, E.; Andres, C.; Buecheler, S.; Tiwari, A. N. High-Efficiency Inverted Semi-Transparent Planar Perovskite Solar Cells in Substrate Configuration. *Nat. Energy* **2017**, *2*, 16190. https://doi.org/10.1038/nenergy.2016.190.

(12)   Leijtens, T.; Bush, K. A.; Prasanna, R.; McGehee, M. D. Opportunities and Challenges for Tandem Solar Cells Using Metal Halide Perovskite Semiconductors. *Nat. Energy* **2018**, *3* (10), 828–838. https://doi.org/10.1038/s41560-018-0190-4.

(13)   Bush, K. A.; Palmstrom, A. F.; Yu, Z. J.; Boccard, M.; Cheacharoen, R.; Mailoa, J. P.; McMeekin, D. P.; Hoye, R. L. Z.; Bailie, C. D.; Leijtens, T.; Peters, I. M.; Minichetti, M. C.; Rolston, N.; Prasanna, R.; Sofia, S.; Harwood, D.; Ma, W.; Moghadam, F.; Snaith, H. J.; Buonassisi, T.; Holman, Z. C.; Bent, S. F.; McGehee, M. D. 23.6%-Efficient Monolithic Perovskite/Silicon Tandem Solar Cells With Improved Stability. *Nat. Energy* **2017**, *2*,

17009. https://doi.org/10.1038/nenergy.2017.9.

(14)   Jošt, M.; Köhnen, E.; Morales-Vilches, A. B.; Lipovšek, B.; Jäger, K.; Macco, B.; Al-Ashouri, A.; Krč, J.; Korte, L.; Rech, B.; Schlatmann, R.; Topič, M.; Stannowski, B.; Albrecht, S. Textured Interfaces in Monolithic Perovskite/Silicon Tandem Solar Cells: Advanced Light Management for Improved Efficiency and Energy Yield. *Energy Environ. Sci.* **2018**, *11* (12), 3511–3523. https://doi.org/10.1039/c8ee02469c.

(15)   Werner, J.; De Wolf, S.; Paviet-Salomon, B.; Nicolay, S.; Bräuninger, M.; Barraud, L.; Ballif, C.; Sacchetto, D.; Despeisse, M.; Walter, A.; Tétreault, N.; Niesen, B.; Sahli, F.; Moon, S.; Allebé, C. Efficient Near-Infrared-Transparent Perovskite Solar Cells Enabling Direct Comparison of 4-Terminal and Monolithic Perovskite/Silicon Tandem Cells. *ACS Energy Letters*. 2016, *1* (2), 474–480. https://doi.org/10.1021/acsenergylett.6b00254.

(16)   Duong, T.; Wu, Y. L.; Shen, H.; Peng, J.; Fu, X.; Jacobs, D.; Wang, E. C.; Kho, T. C.; Fong, K. C.; Stocks, M.; Franklin, E.; Blakers, A.; Zin, N.; McIntosh, K.; Li, W.; Cheng, Y. B.; White, T. P.; Weber, K.; Catchpole, K. Rubidium Multication Perovskite with Optimized Bandgap for Perovskite-Silicon Tandem with over 26% Efficiency. *Adv. Energy Mater.* **2017**, *7* (14), 1700228. https://doi.org/10.1002/aenm.201700228.

(17)   Gnaser, H. Energy and Angular Distributions of Sputtered Species. *Sputtering by particle bombardment*. *Springer,* **2007**, 231–328. https://doi.org/10.1007/978-3-540-44502-9_5.

(18)   You, J.; Meng, L.; Song, T. Bin; Guo, T. F.; Chang, W. H.; Hong, Z.; Chen, H.; Zhou, H.; Chen, Q.; Liu, Y.; De Marco, N.; Yang, Y. Improved Air Stability of Perovskite Solar Cells via Solution-Processed Metal Oxide Transport Layers. *Nat. Nanotechnol.* **2016**, *11* (1), 75–81. https://doi.org/10.1038/nnano.2015.230.

(19)   Bush, K. A.; Bailie, C. D.; Chen, Y.; Bowring, A. R.; Wang, W.; Ma, W.; Leijtens, T.;

Moghadam, F.; McGehee, M. D. Thermal and Environmental Stability of Semi-Transparent Perovskite Solar Cells for Tandems by a Solution-Processed Nanoparticle Buffer Layer and Sputtered ITO Electrode. *2017 IEEE 44th Photovolt. Spec. Conf. PVSC 2017* **2017**, 1850–1854. https://doi.org/10.1109/PVSC.2017.8366593.

(20)   Sahli, F.; Werner, J.; Kamino, B. A.; Bräuninger, M.; Monnard, R.; Paviet-Salomon, B.; Barraud, L.; Ding, L.; Diaz Leon, J. J.; Sacchetto, D.; Cattaneo, G.; Despeisse, M.; Boccard, M.; Nicolay, S.; Jeangros, Q.; Niesen, B.; Ballif, C. Fully Textured Monolithic Perovskite/Silicon Tandem Solar Cells with 25.2% Power Conversion Efficiency. *Nat. Mater.* **2018**, *17* (9), 820–826. https://doi.org/10.1038/s41563-018-0115-4.

(21)   Tong, J.; Song, Z.; Kim, D. H.; Chen, X.; Chen, C.; Palmstrom, A. F.; Ndione, P. F.; Reese, M. O.; Dunfield, S. P.; Reid, O. G.; Liu, J.; Zhang, F.; Harvey, S. P.; Li, Z.; Christensen, S. T.; Teeter, G.; Zhao, D.; Al-Jassim, M. M.; Van Hest, M. F. A. M.; Beard, M. C.; Shaheen, S. E.; Berry, J. J.; Yan, Y.; Zhu, K. Carrier Lifetimes of >1 Ms in Sn-Pb Perovskites Enable Efficient All-Perovskite Tandem Solar Cells. *Science* **2019**, *364* (6439), 475–479. https://doi.org/10.1126/science.aav7911.

(22)   Shen, H.; Duong, T.; Peng, J.; Jacobs, D.; Wu, N.; Gong, J.; Wu, Y.; Karuturi, S. K.; Fu, X.; Weber, K.; Xiao, X.; White, T. P.; Catchpole, K. Mechanically-Stacked Perovskite/CIGS Tandem Solar Cells with Efficiency of 23.9% and Reduced Oxygen Sensitivity. *Energy Environ. Sci.* **2018**, *11* (2), 394–406. https://doi.org/10.1039/c7ee02627g.

(23)   Xu, J.; Boyd, C. C.; Yu, Z. J.; Palmstrom, A. F.; Witter, D. J.; Larson, B. W.; France, R. M.; Werner, J.; Harvey, S. P.; Wolf, E. J.; Weigand, W.; Manzoor, S.; Hest, M. F. A. M. Van; Berry, J. J.; Luther, J. M.; Holman, Z. C.; Mcgehee, M. D. Triple-Halide Wide–Band

Gap Perovskites with Suppressed Phase Segregation for Efficient Tandems. *Science* **2020**, *367* (1104), 1097–1104.

(24)   ITPV. *International Technology Roadmap for Photovoltaics Ninth Edition 2018*; 2019.

(25)   Andrei, V.; Reuillard, B.; Reisner, E. Bias-Free Solar Syngas Production by Integrating a Molecular Cobalt Catalyst with Perovskite–BiVO4 Tandems. *Nat. Mater.* **2019**, *19*, 189–194. https://doi.org/10.1038/s41563-019-0501-6.

(26)   Zhao, D.; Wang, C.; Song, Z.; Yu, Y.; Chen, C.; Zhao, X.; Zhu, K.; Yan, Y. Four-Terminal All-Perovskite Tandem Solar Cells Achieving Power Conversion Efficiencies Exceeding 23%. *ACS Energy Lett.* **2018**, *3* (2), 305–306. https://doi.org/10.1021/acsenergylett.7b01287.

(27)   Kranz, L.; Abate, A.; Feurer, T.; Fu, F.; Avancini, E.; Löckinger, J.; Reinhard, P.; Zakeeruddin, S. M.; Grätzel, M.; Buecheler, S.; Tiwari, A. N. High-Efficiency Polycrystalline Thin Film Tandem Solar Cells. *J. Phys. Chem. Lett.* **2015**, *6* (14), 2676–2681. https://doi.org/10.1021/acs.jpclett.5b01108.

(28)   Hou, Y.; Du, X.; Scheiner, S.; McMeekin, D. P.; Wang, Z.; Li, N.; Killian, M. S.; Chen, H.; Richter, M.; Levchuk, I.; Schrenker, N.; Spiecker, E.; Stubhan, T.; Luechinger, N. A.; Hirsch, A.; Schmuki, P.; Steinrück, H. P.; Fink, R. H.; Halik, M.; Snaith, H. J.; Brabec, C. J. A Generic Interface to Reduce the Efficiency-Stability-Cost Gap of Perovskite Solar Cells. *Science* **2017**, *358* (6367), 1192–1197. https://doi.org/10.1126/science.aao5561.

(29)   Ramos, F. J.; Jutteau, S.; Posada, J.; Bercegol, A.; Rebai, A.; Guillemot, T.; Bodeux, R.; Schneider, N.; Loones, N.; Ory, D.; Broussillou, C.; Goaer, G.; Lombez, L.; Rousset, J. Highly Efficient MoOx-Free Semitransparent Perovskite Cell for 4 T Tandem Application Improving the Efficiency of Commercially-Available Al-BSF Silicon. *Sci. Rep.* **2018**, *8*,

16139. https://doi.org/10.1038/s41598-018-34432-5.

(30)   Raiford, J. A.; Belisle, R. A.; Bush, K. A.; Prasanna, R.; Palmstrom, A. F.; McGehee, M. D.; Bent, S. F. Atomic Layer Deposition of Vanadium Oxide to Reduce Parasitic Absorption and Improve Stability in N-i-p Perovskite Solar Cells for Tandems. *Sustain. Energy Fuels* **2019**, *3* (6), 1517–1525. https://doi.org/10.1039/c9se00081j.

(31)   Park, H. H.; Kim, J.; Kim, G.; Jung, H.; Kim, S.; Moon, C. S.; Lee, S. J.; Shin, S. S.; Hao, X.; Yun, J. S.; Green, M. A.; Ho-baillie, A. W. Y.; Jeon, N. J.; Yang, T.; Seo, J. Transparent Electrodes Consisting of a Surface-Treated Buffer Layer Based on Tungsten Oxide for Semitransparent Perovskite Solar Cells and Four-Terminal Tandem Applications. *Small* **2020**, *4* , 2000074. https://doi.org/10.1002/smtd.202000074.

(32)   Hoye, R. L. Z.; Bush, K. A.; Oviedo, F.; Sofia, S. E.; Thway, M.; Li, X.; Liu, Z.; Jean, J.; Mailoa, J. P.; Osherov, A.; Lin, F.; Palmstrom, A. F.; Bulovic, V.; McGehee, M. D.; Peters, I. M.; Buonassisi, T. Developing a Robust Recombination Contact to Realize Monolithic Perovskite Tandems with Industrially Common P-Type Silicon Solar Cells. *IEEE J. Photovolt.* **2018**, *8* (4), 1023–1028. https://doi.org/10.1109/JPHOTOV.2018.2820509.

(33)   Zhao, B.; Lee, L. C.; Yang, L.; Pearson, A. J.; Lu, H.; She, X. J.; Cui, L.; Zhang, K. H. L.; Hoye, R. L. Z.; Karani, A.; Xu, P.; Sadhanala, A.; Greenham, N. C.; Friend, R. H.; MacManus-Driscoll, J. L.; Di, D. In Situ Atmospheric Deposition of Ultrasmooth Nickel Oxide for Efficient Perovskite Solar Cells. *ACS Appl. Mater. Interfaces* **2018**, *10* (49), 41849–41854. https://doi.org/10.1021/acsami.8b15503.

(34)   Yu, W.; Li, F.; Wang, H.; Alarousu, E.; Chen, Y.; Lin, B.; Wang, L.; Hedhili, M. N.; Li, Y.; Wu, K.; Wang, X.; Mohammed, O. F.; Wu, T. Ultrathin Cu 2 O as an Efficient Inorganic Hole Transporting Material for Perovskite Solar Cells. *Nanoscale* **2016**, *8* (11), 6173–6179.

https://doi.org/10.1039/c5nr07758c.

(35) Palmstrom, A. F.; Raiford, J. A.; Prasanna, R.; Bush, K. A.; Sponseller, M.; Cheacharoen, R.; Minichetti, M. C.; Bergsman, D. S.; Leijtens, T.; Wang, H. P.; Bulović, V.; McGehee, M. D.; Bent, S. F. Interfacial Effects of Tin Oxide Atomic Layer Deposition in Metal Halide Perovskite Photovoltaics. *Adv. Energy Mater.* **2018**, *8* (23), 1800591. https://doi.org/10.1002/aenm.201800591.

(36) Ciro, J.; Ramírez, D.; Mejía Escobar, M. A.; Montoya, J. F.; Mesa, S.; Betancur, R.; Jaramillo, F. Self-Functionalization behind a Solution-Processed NiOx Film Used As Hole Transporting Layer for Efficient Perovskite Solar Cells. *ACS Appl. Mater. Interfaces* **2017**, *9* (14), 12348–12354. https://doi.org/10.1021/acsami.6b15975.

(37) Koushik, D.; Jošt, M.; Dučinskas, A.; Burgess, C.; Zardetto, V.; Weijtens, C.; Verheijen, M. A.; Kessels, W. M. M.; Albrecht, S.; Creatore, M. Plasma-Assisted Atomic Layer Deposition of Nickel Oxide as Hole Transport Layer for Hybrid Perovskite Solar Cells. *J. Mater. Chem. C* **2019**, *7* (40), 12532–12543. https://doi.org/10.1039/c9tc04282b.

(38) Chen, Y. J.; Li, M. H.; Huang, J. C. A.; Chen, P. Cu/Cu2O Nanocomposite Films as a p-Type Modified Layer for Efficient Perovskite Solar Cells. *Sci. Rep.* **2018**, *8* ,7646. https://doi.org/10.1038/s41598-018-25975-8.

(39) Thway, M.; Liu, T.; Huang, M.; Ke, C.; Ng, X. R.; Nagarajan, B.; Yan, X.; Duttagupta, S.; Stangl, R.; Chua, S. J.; Aberle, A. G.; Lin, F. Small-Area p-Type PERC Silicon Solar Cells for Tandem Applications. In *Light, Energy and the Environment Congress*; OSA Publishing: Singapore, 2018. https://doi.org/10.1364/OSE.2018.OT3C.4.

(40) Duttagupta, S.; Nandakumar, N.; Padhamnath, P.; Buatis, J. K.; Stangl, R.; Aberle, A. G. MonoPoly™ Cells: Large-Area Crystalline Silicon Solar Cells with Fire-through Screen

Printed Contact to Doped Polysilicon Surfaces. *Sol. Energy Mater. Sol. Cells* **2018**, *187* (1), 76–81. https://doi.org/10.1016/j.solmat.2018.05.059.

(41)   Iivonen, T.; Heikkila, M. J.; Popov, G.; Nieminen, H.; Kaipio, M.; Kemell, M.; Mattinen, M.; Mizohata, K.; Ritala, M. Atomic Layer Deposition of Photoconductive Cu 2 O Thin Films. *ACS Omega* **2019**, *4* (6) , 11205–11214. https://doi.org/10.1021/acsomega.9b01351.

(42)   Hoye, R. L. Z.; Muñoz-Rojas, D.; Musselman, K. P.; Vaynzof, Y.; MacManus-Driscoll, J. L. Synthesis and Modeling of Uniform Complex Metal Oxides by Close-Proximity Atmospheric Pressure Chemical Vapor Deposition. *ACS Appl. Mater. Interfaces* **2015**, *7* (20), 10684–10694. https://doi.org/10.1021/am5073589.

(43)   Raninga, R. D.; Jagt, R. A.; Béchu, S.; Huq, T. N.; Nikolka, M.; Lin, Y.-H.; Sun, M.; Li, Z.; Li, W.; Bouttemy, M.; Frégnaux, M.; Snaith, H. J.; Schulz, P.; MacManus-Driscoll, J. L.; Hoye, R. L. Z. Strong Performance Enhancement in Lead-Halide Perovskite Solar Cells through Rapid, Atmospheric Deposition of n-Type Buffer Layer Oxides. *Nano Energy* **2020**, 104946. https://doi.org/10.1016/j.nanoen.2020.104946

(44)   Muñoz-Rojas, D.; Jordan, M.; Yeoh, C.; Marin, A. T.; Kursumovic, A.; Dunlop, L. A.; Iza, D. C.; Chen, A.; Wang, H.; MacManus Driscoll, J. L. Growth of ∼5 Cm2V-1s-1 Mobility, p-Type Copper(I) Oxide (Cu2O) Films by Fast Atmospheric Atomic Layer Deposition (AALD) at 225°C and Below. *AIP Adv.* **2012**, *2*, 042179. https://doi.org/10.1063/1.4771681.

(45)   Schmidt-Whitley, R. D.; Martinez-Clemente, M.; Revcolevschi, A. Growth and Microstructural Control of Single Crystal Cuprous Oxide Cu2O. *J. Cryst. Growth* **1974**, *23* (2), 113–120. https://doi.org/10.1016/0022-0248(74)90110-9.

(46)   Hoye, R. L. Z.; Brandt, R. E.; Ievskaya, Y.; Heffernan, S.; Musselman, K. P.; Buonassisi,

T.; Macmanus-Driscoll, J. L. Perspective: Maintaining Surface-Phase Purity Is Key to Efficient Open Air Fabricated Cuprous Oxide Solar Cells. *APL Mater*. **2015**, *3* , 020901. https://doi.org/10.1063/1.4913442.

(47)   Choudhary, S.; Sarma, J. V. N.; Pande, S.; Ababou-girard, S.; Turban, P.; Lepine, B.; Gangopadhyay, S. Oxidation Mechanism of Thin Cu Films : A Gateway towards the Formation of Single Oxide Phase. *AIP Adv*. **2018**, *8*, 055114. https://doi.org/10.1063/1.5028407.

(48)   Wang, Y.; Miska, P.; Pilloud, D.; Horwat, D.; Pierson, J. F. Transmittance Enhancement and Optical Band Gap Widening of Cu 2 O Thin Films after Air Annealing. *J. Appl. Phys*. **2014**, *115* (7) , 073505. https://doi.org/10.1063/1.4865957.

(49)   Jacobsson, T. J.; Correa-Baena, J. P.; Halvani Anaraki, E.; Philippe, B.; Stranks, S. D.; Bouduban, M. E. F.; Tress, W.; Schenk, K.; Teuscher, J.; Moser, J. E.; Rensmo, H.; Hagfeldt, A. Unreacted PbI2 as a Double-Edged Sword for Enhancing the Performance of Perovskite Solar Cells. *J. Am. Chem. Soc*. **2016**, *138* (32), 10331–10343. https://doi.org/10.1021/jacs.6b06320.

(50)   Calió, L.; Kazim, S.; Grätzel, M.; Ahmad, S. Hole-Transport Materials for Perovskite Solar Cells. *Angew. Chem. Int. Ed*. **2016**, *55* (47), 14522–14545. https://doi.org/10.1002/anie.201601757; *Angew. Chem*. **2016**, *128* (47), 14740-14764. https://doi.org/10.1002/ange.201601757

(51)   Stranks, S. D. Nonradiative Losses in Metal Halide Perovskites. *ACS Energy Lett*. **2017**, *2* (7), 1515–1525. https://doi.org/10.1021/acsenergylett.7b00239.

(52)   Abdi-Jalebi, M.; Andaji-Garmaroudi, Z.; Cacovich, S.; Stavrakas, C.; Philippe, B.; Richter, J. M.; Alsari, M.; Booker, E. P.; Hutter, E. M.; Pearson, A. J.; Lilliu, S.; Savenije, T. J.;

Rensmo, H.; Divitini, G.; Ducati, C.; Friend, R. H.; Stranks, S. D. Maximizing and Stabilizing Luminescence from Halide Perovskites with Potassium Passivation. *Nature* **2018**, *555* (7697), 497–501. https://doi.org/10.1038/nature25989.

(53) Musselman, K. P.; Muñoz-Rojas, D.; Hoye, R. L. Z.; Sun, H.; Sahonta, S. L.; Croft, E.; Böhm, M. L.; Ducati, C.; MacManus-Driscoll, J. L. Rapid Open-Air Deposition of Uniform, Nanoscale, Functional Coatings on Nanorod Arrays. *Nanoscale Horiz.* **2017**, *2* (2), 110–117. https://doi.org/10.1039/c6nh00197a.

(54) Tsarev, S.; Yakushchenko, I. K.; Luchkin, S. Y.; Kuznetsov, P. M.; Timerbulatov, R. S.; Dremova, N. N.; Frolova, L. A.; Stevenson, K. J.; Troshin, P. A. A New Polytriarylamine Derivative for Dopant-Free High-Efficiency Perovskite Solar Cells. *Sustain. Energy Fuels* **2019**, *3* (10), 2627–2632. https://doi.org/10.1039/c9se00448c.

(55) Chen, B.; Bai, Y.; Yu, Z.; Li, T.; Zheng, X.; Dong, Q.; Shen, L.; Boccard, M.; Gruverman, A.; Holman, Z.; Huang, J. Efficient Semitransparent Perovskite Solar Cells for 23.0%-Efficiency Perovskite/Silicon Four-Terminal Tandem Cells. *Adv. Energy Mater.* **2016**, *6* (19), 1601128. https://doi.org/10.1002/aenm.201601128.

(56) Dewi, H. A.; Wang, H.; Li, J.; Thway, M.; Sridharan, R.; Stangl, R.; Lin, F.; Aberle, A. G.; Mathews, N.; Bruno, A.; Mhaisalkar, S. Highly Efficient Semitransparent Perovskite Solar Cells for Four Terminal Perovskite-Silicon Tandems. *ACS Appl. Mater. Interfaces* **2019**, *11* (37), 34178–34187. https://doi.org/10.1021/acsami.9b13145.

(57) Ramírez Quiroz, C. O.; Shen, Y.; Salvador, M.; Forberich, K.; Schrenker, N.; Spyropoulos, G. D.; Heumüller, T.; Wilkinson, B.; Kirchartz, T.; Spiecker, E.; Verlinden, P. J.; Zhang, X.; Green, M. A.; Ho-Baillie, A.; Brabec, C. J. Balancing Electrical and Optical Losses for Efficient 4-Terminal Si-Perovskite Solar Cells with Solution Processed Percolation

Electrodes. *J. Mater. Chem. A* **2018**, *6* (8), 3583–3592. https://doi.org/10.1039/c7ta10945h.

(58) Kim, D.; Kim, D.; Jung, H. J.; Park, I. J.; Larson, B. W.; Dunfield, S. P.; Xiao, C.; Kim, J.; Tong, J.; Boonmongkolras, P.; Ji, S. G.; Zhang, F.; Pae, S. R. Efficient , Stable Silicon Tandem Cells Enabled by Anion- Engineered Wide-Bandgap Perovskites. *Science* **2020**, *368* (6487), 155-160. https://doi.org/10.1126/science.aba3433

(59) Duong, T.; Pham, H.; Kho, T. C.; Phang, P.; Fong, K. C.; Yan, D.; Yin, Y.; Peng, J.; Mahmud, A.; Gharibzadeh, S.; Nejand, B. A.; Hossain, I. M.; Khan, M. R.; Mozaffari, N.; Wu, Y.; Shen, H.; Zheng, J.; Mai, H.; Liang, W.; Samundsett, C.; Stocks, M.; Mcintosh, K.; Andersson, G. G.; Lemmer, U.; Richards, B. S.; Paetzold, U. W.; Ho-ballie, A.; Liu, Y.; Macdonald, D.; Blakers, A.; Wong-leung, J.; White, T.; Weber, K.; Catchpole, K. High Efficiency Perovskite-Silicon Tandem Solar Cells : Effect of Surface Coating versus Bulk Incorporation of 2D Perovskite. *Adv. Energy Mater.* **2020**, *10*, 1903553. https://doi.org/10.1002/aenm.201903553.

(60) Guo, Y.; Lei, H.; Xiong, L.; Li, B.; Fang, G. An Integrated Organic-Inorganic Hole Transport Layer for Efficient and Stable Perovskite Solar Cells. *J. Mater. Chem. A* **2018**, *6* (5), 2157–2165. https://doi.org/10.1039/c7ta09946k.

(61) Yoshikawa, K.; Kawasaki, H.; Yoshida, W.; Irie, T.; Konishi, K.; Nakano, K.; Uto, T.; Adachi, D.; Kanematsu, M.; Uzu, H.; Yamamoto, K. Silicon Heterojunction Solar Cell with Interdigitated Back Contacts for a Photoconversion Efficiency over 26%. *Nat. Energy* **2017**, *2*, 17032. https://doi.org/10.1038/nenergy.2017.32.

(62) Jaysankar, M.; Raul, B. A. L.; Bastos, J.; Burgess, C.; Weijtens, C.; Creatore, M.; Aernouts, T.; Kuang, Y.; Gehlhaar, R.; Hadipour, A.; Poortmans, J. Minimizing Voltage Loss in Wide-Bandgap Perovskites for Tandem Solar Cells. *ACS Energy Lett.* **2019**, *4* (1), 259–264.

https://doi.org/10.1021/acsenergylett.8b02179.

(63)   Bush, K. A.; Manzoor, S.; Frohna, K.; Yu, Z. J.; Raiford, J. A.; Palmstrom, A. F.; Wang, H.; Prasanna, R.; Bent, S. F.; Holman, Z. C.; Mcgehee, M. D. Minimizing Current and Voltage Losses to Reach 25 % -Efficient Monolithic Two-Terminal Perovskite-Silicon Tandem Solar Cells. *ACS Energy Lett*. **2018**, *3* (9), 2173–2180. https://doi.org/10.1021/acsenergylett.8b01201.

(64)   Werner, J.; Geissbühler, J.; Dabirian, A.; Nicolay, S.; Morales-Masis, M.; Wolf, S. De; Niesen, B.; Ballif, C. Parasitic Absorption Reduction in Metal Oxide-Based Transparent Electrodes: Application in Perovskite Solar Cells. *ACS Appl*. *Mater*. *Interfaces* **2016**, *8* (27), 17260–17267. https://doi.org/10.1021/acsami.6b04425.

(65)   Liu, W.; Cheng, S. Photoelectric Properties of ITO Thin Films Deposited by DC Magnetron Sputtering. *J*. *Semicond*. **2011**, *32* (1), 013002. https://doi.org/10.1088/1674-4926/32/1/013002.